

Nanoscale scanning probe ferromagnetic resonance imaging using localized modes

Inhee Lee¹, Yuri Obukhov¹, Gang Xiang¹, Adam Hauser¹, Fengyuan Yang¹, Palash Banerjee¹, Denis V. Pelekhov¹ & P. Chris Hammel¹

The discovery of new phenomena in layered and nanostructured magnetic devices is driving rapid growth in nanomagnetism research. Resulting applications such as giant magnetoresistive field sensors and spin torque devices are fuelling advances in information and communications technology, magnetoelectronic sensing and biomedicine^{1,2}. There is an urgent need for high-resolution magnetic-imaging tools capable of characterizing these complex, often buried, nanoscale structures. Conventional ferromagnetic resonance^{3,4} (FMR) provides quantitative information about ferromagnetic materials and interacting multicomponent magnetic structures with spectroscopic precision and can distinguish components of complex bulk samples through their distinctive spectroscopic features. However, it lacks the sensitivity to probe nanoscale volumes and has no imaging capabilities. Here we demonstrate FMR imaging through spin-wave localization. Although the strong interactions in a ferromagnet favour the excitation of extended collective modes, we show that the intense, spatially confined magnetic field of the micromagnetic probe tip used in FMR force microscopy can be used to localize the FMR mode immediately beneath the probe. We demonstrate FMR modes localized within volumes having 200 nm lateral dimensions, and improvements of the approach may allow these dimensions to be decreased to tens of nanometres. Our study shows that this approach is capable of providing the microscopic detail required for the characterization of ferromagnets used in fields ranging from spintronics to biomagnetism. This method is applicable to buried and surface magnets, and, being a resonance technique, measures local internal fields and other magnetic properties with spectroscopic precision.

Scanning probe FMR, or FMR force microscopy^{5–7} (FMRFM), is based on magnetic resonance force microscopy (MRFM)^{8–10} in which magnetic resonance is sensitively detected through the magnetic dipole force exerted on a cantilever by means of a micromagnetic tip (see Fig. 1a for a schematic diagram). MRFM has demonstrated the sensitivity necessary to study nanoscale objects^{5,6,11}. In a paramagnet, the resonance frequency of a spin is a local function of the applied field. MRFM exploits this (as does magnetic resonance imaging) to localize the resonant excitation controllably through an applied magnetic field gradient that establishes a correlation between position and frequency. This approach is not applicable in a ferromagnet, however, because the strong interactions among spins render the precession frequency at a particular location sensitive to the magnetization of the remainder of the sample. Excitations in a ferromagnet are thus collective modes^{3,4}, so magnetic resonance imaging in a ferromagnet requires the localization of these spin-wave modes.

Spin waves can be localized by the strongly inhomogeneous internal field in patterned ferromagnetic film structures¹², and standing spin waves inside magnetic wells have been discussed theoretically¹³. A

spin-polarized current injected into a ferromagnetic film generates a localized spin-wave mode¹⁴ beneath the electrode, but these cannot be scanned for imaging. Confining the excitation of FMR modes within boundaries defined by a scannable micromagnetic probe field has been proposed^{15,16}; here we report the observation of localized modes induced by the micromagnetic probe tip and use them for scanning probe FMR imaging in ferromagnetic films as schematically indicated Fig. 1a.

For a sufficiently weak probe field, $H_p(r, z)$, the magnetostatic mode shape will be negligibly perturbed (see refs 16, 17 for a discussion of the weak-probe-field limit), and the effect of this or any other spatially varying field on the FMR will be given by the spatial average, $\langle H(r) \rangle$, of the field weighted by the mode it is perturbing:

$$\langle H_p(z, r) \rangle_n = \frac{\int_S H_p(r-r', z) m_n^2(r') dS'}{\int_S m_n^2(r') dS'} \equiv \frac{H_p(r, z) * m_n^2(r)}{\int_S m_n^2(r') dS'} \quad (1)$$

Here the asterisk indicates convolution, and $m_n(r)$ are the unperturbed magnetostatic modes. The dynamic magnetization for these modes can be written $m_n(r) = m_{0,n} J_0(\alpha_n r / R_{\text{dot}})$, where J_0 is a Bessel function, $m_{0,n}$ is a constant describing the amplitude of the mode, α_n is the n th zero of J_0 and R_{dot} is the dot radius^{18,19}. The probe field experienced by the sample becomes small and the weak-perturbation limit is applicable when the tip-sample separation, z , significantly exceeds the $\sim 1\text{-}\mu\text{m}$ tip dimension (Fig. 1a, c).

However, when the probe field exceeds the transverse dipolar field ($\sim 2\pi M_s(t/R_{\text{dot}})$) for a ferromagnetic disk of thickness t and saturation magnetization M_s it will localize modes. Here we consider a negative probe field that will produce a local field 'well'. The analogy²⁰ between the linearized Landau–Lifshitz equation for exchange spin waves and the Schrödinger equation provides useful intuition and guidance in understanding the mechanism by which an intense micromagnetic probe field can localize spin waves: the non-uniform probe magnetic field produces a region of reduced magnetic field analogous to the potential well that confines particles. Similarly, the Landau–Lifshitz spin-wave equation has a localized solution as illustrated in Fig. 1b. In the case of dipole and dipole-exchange spin waves, the situation considered here, the Landau–Lifshitz equation is a more complex integro-differential problem requiring micromagnetic modelling for accurate solution in many cases. Such modelling¹⁶ finds a localized solution as illustrated in Fig. 1b.

The FMRFM spectra obtained from extended films, shown in Fig. 1c, demonstrate that magnetostatic modes have been confined by the localized magnetic field of the high-coercivity ($>2\text{ T}$) SmCo_5 probe tip. These experiments were performed on a continuous permalloy film of thickness $t = 40\text{ nm}$ in an applied field, H_0 , perpendicular to the film plane, antiparallel to the tip moment, m_p , and sufficient to saturate the film. The tip creates a well of magnetic field in the saturated film as illustrated in Fig. 1b.

¹Department of Physics, Ohio State University, Columbus, Ohio 43210, USA.

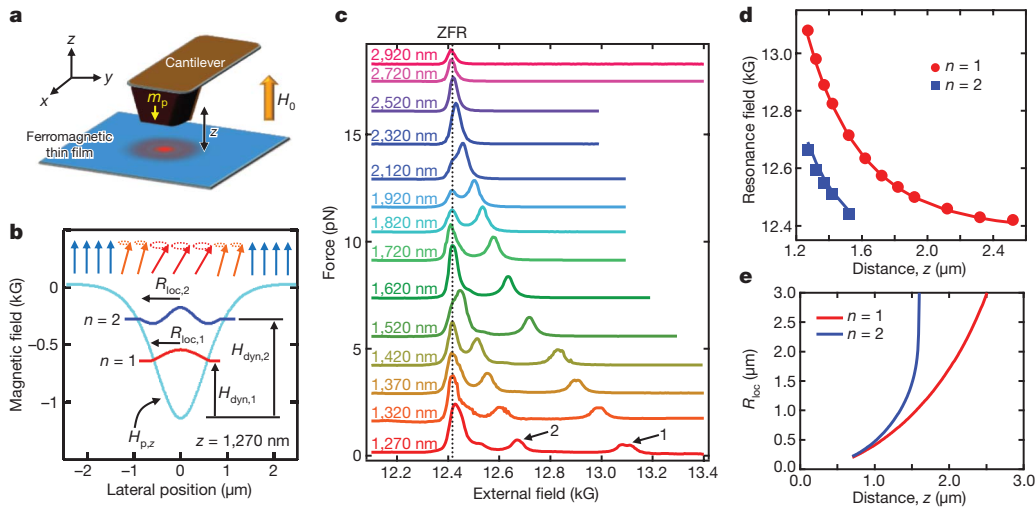


Figure 1 | Observation and characterization of localized FMR modes.

a, FMRFM geometry: the ferromagnetic film is magnetized perpendicular to its plane by an external magnetic field, H_0 . The moment, m_p , of the micromagnetic probe is antiparallel to H_0 and is separated from the film by a distance z (the distance from the surface to the centre of the probe magnet). **b**, The micromagnetic probe creates a well of magnetic field, shown by the solid light-blue line, that localizes spin-wave excitations $m_{loc,n}(r)$, indicated by the solid red and blue lines for the first two modes. The probe field (H_p),

The conventional FMR spectrum of a saturated, continuous ferromagnetic film consists of a single resonance peak; in Fig. 1c, this uniform FMR mode peak occurs at $H_{res} = 12.41$ kG and is labelled ZFR¹⁶ (zero probe field resonance). As the probe approaches the sample, new discrete resonances appear and shift to higher field values as the negative probe field increases in strength. These are similar to the discrete FMR modes observed in patterned films, where the structure's dimensions define the wavevectors of the magnetostatic modes^{19,21,22}. However, in an extended, saturated, thin ferromagnetic film, these additional discrete FMR modes can only be due to modes with wavevectors defined by confinement within the region of intense micromagnetic probe field.

The FMR modes are confined immediately beneath the probe, where they benefit from the locally reduced field; however, confinement is opposed by the increasing exchange and dipolar energies associated with the increased wavevector of the confined mode. The trade-off between these effects is optimized for a particular value of the radius of the confined mode, $R_{loc,n}$. This radius determines the resulting shift of the FMR peak from the zero probe field resonance as shown in Fig. 1c; this shift is indicated schematically in Fig. 1b by the difference in the vertical positions of the baselines of the FMR modes drawn in the calculated field well. We calculate $R_{loc,n}$ using a variational technique in which $R_{loc,n}$ is varied until the mode frequency, ω , determined from the dispersion relation of ref. 23 with corrections for non-uniform fields^{16,21} (equation (4)), is minimized. For a sufficiently strong negative probe field (that is, sufficiently small tip-sample separation, z) $R_{loc,n}$ rapidly decreases (Fig. 1e) and the mode localizes.

To calculate $R_{loc,m}$ we assume the usual Bessel mode expansion^{18,19}: $m_{loc,n}(r) = m_{0,n}J_0(\alpha_n r/R_{loc,n})$. Here α_n is the n th zero of the Bessel function ($J_0(\alpha_n) = 0$); micromagnetic simulations¹⁶ confirm that $R_{loc,n}$ is distinct for each mode. We vary the single free parameter, $R_{loc,m}$ until ω is minimized. The spatial variation in the probe field at each probe-sample separation is taken to be that of a point dipole, the moment of which is known from cantilever magnetometry (see equation (44) in ref. 7); a single, fixed value of the location of the point dipole relative to the surface of the probe magnet is used for all values of z and n . Once $R_{loc,n}$ is determined (Fig. 1e), we calculate the resonance fields for the modes (equation (4)); these are shown as solid lines in Fig. 1d. The excellent agreement with experimental data demonstrates the validity of our variational approach.

the dynamic field (H_{dyn}) and the modes are calculated for $z = 1,270$ nm. **c**, FMRFM spectra of a continuous permalloy film for the indicated values of z . The vertical dotted line shows the resonance field for the uniform FMR mode (ZFR). The first and second confined modes are indicated by the arrows. **d**, Dependence on z of the resonance fields for the first and second FMR modes. The solid lines are calculations obtained from the variational method described in the text. **e**, Calculated local-mode radius, $R_{loc,n}$, versus z for the first two magnetostatic modes obtained using the variational method.

The demagnetizing field, H_d , of a thin-film ferromagnetic structure (in our case a disk of radius $R_{dot} = 2.12$ μm and thickness $t = 40$ nm) decreases rapidly near its edge, and this provides a convenient test of the ability of the scanned local mode to resolve spatial variations in the internal field. Figure 2 shows the spatial variation in the shift of the resonance field for the localized modes generated at different probe-sample separations. The rightmost four images compare experimental data with theoretical predictions obtained if we neglect the localization of the magnetostatic modes by the probe field, calculated using equation (1) (see also equation (5)).

The dispersion relation for small in-plane wavevectors k in the dot²³ ($kt \ll 1$) gives the dependence of resonance frequency on applied field and various parameters (see Methods, equation (4)). The resonance field, H_{res} , is the applied field, H_0 , at which resonance occurs for the given applied microwave frequency, ω :

$$H_{res} \approx \frac{\omega}{|\gamma|} - \langle H_p \rangle - \langle H_d \rangle - 4\pi M_s \alpha_{ex} k^2 - \pi M_s k t \quad (2)$$

Here γ is the electronic gyromagnetic ratio, $\alpha_{ex} = A/2\pi M_s^2$ and A is the exchange constant. Hence, in the weak-probe-field limit, decreasing z increases the negative probe field $\langle H_p \rangle$, which increases the resonance field as seen in Fig. 2.

As the probe-sample separation becomes small, however, $H_p(r)$ becomes large enough that this approach fails to describe the experimental data, and it becomes necessary to take mode localization into account. The leftmost three images in Fig. 2 compare experimental data with predictions made taking into account the confinement of the magnetostatic modes to within the radius $R_{loc,m}$ obtained by the variational method described above. The mode is scanned with the probe tip, and the variation in H_{res} (equation (2)) is determined by the spatial average of $H_d(r)$ weighted by the localized mode generated at the particular probe height, z :

$$\langle H_d(z, r) \rangle_n = \frac{H_d(r) * m_{loc,n}^2(z, r)}{\int_S m_{loc,n}^2(z, r') dS'} \quad (3)$$

We observe that the shift of the first localized mode increasingly accurately images the non-uniform demagnetizing field, $H_d(r)$, in the dot as z decreases, hence reducing $R_{loc,n}$.

Our theoretical estimate for the first-order localized mode (Fig. 2, solid red line) agrees very closely with the experimental data to the smallest values of z . However, our simplified analytical model is

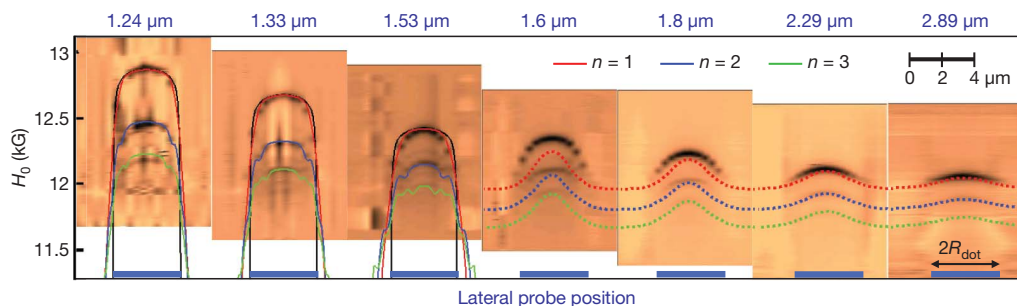


Figure 2 | Field-position FMRFM imaging of a permalloy dot using localized modes. FMRFM images of the FMR resonance shift (such as shown in Fig. 1c) at different lateral positions over the dot (indicated by the thick blue bar), measured for a series of probe-sample separations. These separations describe the distance from the centre of the probe tip to the sample surface, so the bottom of the probe is approximately 350 nm from the surface at the smallest separation shown. The rightmost four panels compare theoretical expectations (dotted lines) assuming no modification of FMR modes by the probe field (equation (1)). Although it is adequate at large separation (weak

limited when FMR modes defined by the probe field reach the dot edge, where the very rapid spatial variation in the demagnetizing field significantly distorts the FMR modes. This limitation is visible for second- and third-order modes. We note, however, that at close probe approach the resonance field of the first-order localized mode (red solid line) coincides very closely with the well-known and straightforwardly calculable demagnetizing field of the dot, shown by the solid black line in Fig. 2. Thus, the first-order local mode accurately visualizes the internal fields of the thin ferromagnetic dot.

We can apply localized-mode FMR imaging as a highly sensitive internal-field sensor that can probe not only demagnetizing fields but also internal fields such as crystalline/surface anisotropy fields, exchange fields in buried structures and even stray fields from external magnetic sources. Figure 3 shows a localized-mode field-position FMR image of the internal fields in our continuous permalloy film for $z = 1.32 \mu\text{m}$. The lateral variation in the resonance fields of the

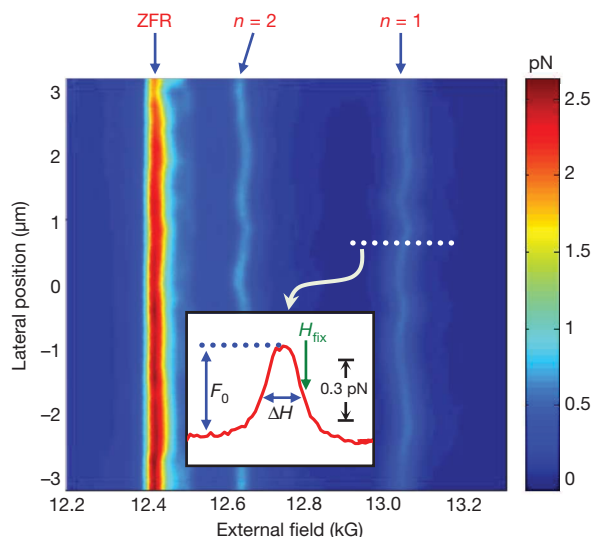


Figure 3 | Field-position FMRFM image of a continuous permalloy film. Variation in the resonance fields of the $n = 1$ and $n = 2$ localized modes with lateral position, for $z = 1.32 \mu\text{m}$, reflecting variation in the internal field in a permalloy film (see text). The inset shows a section through the $n = 1$ mode for a fixed lateral position. By setting the external field to H_{fix} , such that the variation in the FMRFM signal with internal field is a maximum, we realize a high-sensitivity detector of the internal field as a function of x - y position. Variations in the detected force, $\delta F(x, y)$, reflect internal field variations through shifts in the resonance field: $\delta H(x, y) \approx \delta F(x, y) (\Delta H / F_0)$, where ΔH is the FMR linewidth and F_0 is the FMRFM force at resonance. Images obtained by this method are shown in Fig. 4a and in Supplementary Fig. 5a.

probe field), this approach fails upon closer probe approach. The leftmost three images show comparison with confined-mode predictions (coloured solid lines) using variationally calculated values, $R_{\text{loc},n}$ (equation (3)), for the probe-localized magnetostatic mode. The black solid line shows the inhomogeneous demagnetizing field of the dot (shifted by appropriate dynamic and probe fields) corresponding to the first local mode (equation (5)), demonstrating that the first-order localized mode accurately images the internal magnetic field of the dot.

localized modes ($n = 1, 2$), repeatable from measurement to measurement, reflects variations in the saturation magnetization or crystalline anisotropy, or the film roughness.

A two-dimensional internal-field image is obtained by setting the external field to H_{fix} , where the slope, $\partial F / \partial H$, of the FMRFM signal as a function of field for the first-order localized mode is maximum (Fig. 3, inset), and then monitoring the spatial variation in the force signal. Variations in the internal field will shift the resonance peak by δH , thus changing the FMRFM force: $\delta F = (\partial F / \partial H) \delta H$. The field resolution is approximately $\Delta H (F_n / F_0) \approx 1 \text{ G}$, where ΔH is the spectral linewidth ($\sim 50 \text{ G}$) and the signal-to-noise ratio is $F_0 / F_n \approx 100$ for the line shown in the inset in Fig. 3.

Figure 4a shows internal-field images for the permalloy film for different values of z . The variation in the internal field $\delta H(x, y)$ with lateral position is reproducible and persists for different values of z , showing that it reflects inhomogeneity of the sputter-deposited film. As shown in Supplementary Information, the FMRFM images have higher lateral resolution than simultaneously acquired magnetic force microscopy images as a consequence of the very different natures of FMR imaging and magnetic force microscopy: the first measures the internal fields inside a ferromagnetic material whereas the latter maps stray field gradients outside the sample.

These data allow us to characterize our lateral resolution. We determine the maximum resolved wavevector, k_m , from a Fourier transform of the images: 75% of the signal energy in the Fourier transform comes from wavevectors less than k_m . This quantifies the real-space resolution, $R_{\text{res}} = \alpha_1 / k_m$; we become increasingly unable to

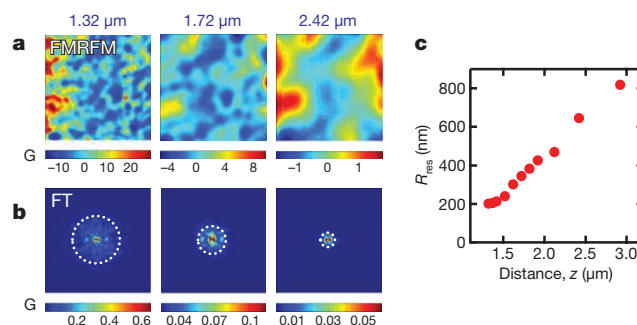


Figure 4 | Two-dimensional x - y FMRFM images of a continuous permalloy film. **a**, FMRFM images of $\delta H(x, y)$ measured at the indicated tip-sample separations. The image size is $6 \mu\text{m} \times 6 \mu\text{m}$. **b**, Dependence of the FMRFM signal on wavevector, obtained from Fourier transform (FT) of the images in **a**; the panel dimensions are $60 \mu\text{m}^{-1} \times 60 \mu\text{m}^{-1}$. Seventy-five per cent of the signal energy is enclosed within the dotted circles. **c**, Dependence of resolution on probe-sample separation, obtained from experimental FMRFM images.

discern lateral variations in sample properties occurring on length scales below R_{res} . Figure 4b shows k_m values (indicated by the radii of the dotted circles) determined from Fourier transforms at several probe-sample separations, and we plot the dependence of the lateral resolution on probe-sample separation in Fig. 4c. Spatial resolution is further discussed in Supplementary Information.

The finest experimental resolution (obtained at $z = 1.3 \mu\text{m}$) is 200 nm. This is consistent with the size of the mode shown in Fig. 1b (see also the discussion in Supplementary Information); a lateral displacement of the tip from a signal source equal to one-third of the mode radius (~ 200 nm in the case shown in Fig. 1b) reduces the signal by 36%, which is large in comparison with the ratio of noise to signal. Spatial resolution is improved by the fact that the detected signal is proportional to $m_n^2(r)$, which drops off more steeply with r . The ultimate resolution will be limited by exchange interactions and can be evaluated (equation (5)). To do so, we ignore the dynamic dipolar field because it can be reduced by decreasing the film thickness, and evaluate the limit defined by the exchange term $R_{\text{loc}} \geq \alpha_1 \sqrt{2A/|H_p(0)|M_s}$, where $|H_p(0)|$ is the maximum probe field; we find that $R_{\text{loc}} > 30$ nm for permalloy. A more detailed calculation of the point response function including the dipolar dynamic field and a complete analysis of the mode characteristics indicates that a resolution of $R_{\text{res}} \approx 90$ nm is achievable in a 40-nm-thick permalloy film.

The localized FMR mode can also be viewed as a detector of external magnetic fields with a sensitivity of $\sim 1 \text{ GHz}^{-1/2}$ in a sensor area of radius ~ 200 nm, that is, a detected volume of $\sim 5 \times 10^{-21} \text{ m}^3$. This field sensitivity can be straightforwardly improved by using a ferromagnetic film with a narrower FMR linewidth, and the effective volume can be decreased by reducing the moment of the magnetic probe and optimizing the ferromagnetic film parameters (Supplementary Information). Our technique provides a readily applicable approach to the high-resolution imaging of (possibly buried) magnetic structures, such as those used in spintronic, sensing and biomagnetic applications, with spectroscopic precision.

METHODS SUMMARY

A high-coercivity (>2 T) SmCo_5 micromagnetic probe, with volume $\sim 1.2 \times 1.2 \times 1.5 \mu\text{m}^3$ and moment $m_p = 1.2 \times 10^{-9}$ e.m.u. oriented antiparallel to the applied field, creates a well of magnetic field in the film as illustrated in Fig. 1b. The applied field, which is sufficient to saturate the film, is applied perpendicular to the film plane (the z direction) as shown in Fig. 1a. We attach the probe to a silicon cantilever (spring constant, $k_s \approx 0.1 \text{ N m}^{-1}$), and through the magnetic dipolar interaction it detects the FMR excitations in the sample. Details of the FMRFM technique are available in refs 5, 7, 16, 22, 24. Our experiments were performed on a continuous permalloy film and a permalloy disk of radius $R_{\text{dot}} = 2.12 \mu\text{m}$, both $t = 40$ nm thick.

The experiments were performed at 10 K, the microwave frequency was 7.475 GHz; we modulated the amplitude of the microwaves at the cantilever frequency to generate a modulated force detectable by the cantilever. The magnetic moment of the tip was determined from cantilever magnetometry; its dipolar field can be easily calculated from this moment. The probe field at $z = 1.3 \mu\text{m}$ was ~ 1.2 kG (Fig. 1b) and decreased monotonically as $1/z^3$ with increasing z .

The dispersion relation for a thin ferromagnetic film magnetized perpendicular to the film plane is^{21,23}

$$\left(\frac{\omega}{\gamma}\right)^2 = (\langle H_{\text{eff}} \rangle + 4\pi M_s \alpha_{\text{ex}} k^2) (\langle H_{\text{eff}} \rangle + 4\pi M_s \alpha_{\text{ex}} k^2 + 4\pi M_s f(k)) \quad (4)$$

where $H_{\text{eff}} = H_0 - 4\pi M_s + H_p$ is the effective field (we consider only the z component of the fields, because other components are small in comparison with H_{eff}) and $f(k) = 1 - (1 - e^{-kt})/kt$. Here we have taken into account the fact that the field is non-uniform^{16,21}:

$$\langle H_{\text{eff}} \rangle = \frac{\int_S H_{\text{eff}}(r) m^2(r) dS}{\int_S m^2(r) dS}$$

where $m(r)$ is an eigenmode solution for the non-uniform field $H_{\text{eff}}(r)$.

For small wavevectors ($kt \ll 1$), equation (4) can be written

$$\frac{\omega}{|\gamma|} \approx \langle H_{\text{eff}} \rangle + 4\pi M_s \alpha_{\text{ex}} k^2 + \pi M_s k t \quad (5)$$

where, for the continuous film, $\langle H_{\text{eff}} \rangle = H_0 - 4\pi M_s + \langle H_p \rangle$ and, for the dot, $\langle H_{\text{eff}} \rangle = H_0 + \langle H_d \rangle + \langle H_p \rangle$, where $H_d(r)$ is the non-uniform demagnetizing field of the dot.

Received 18 February; accepted 14 June 2010.

1. Wolf, S. A. *et al.* Spintronics: a spin-based electronics vision for the future. *Science* **294**, 1488–1495 (2001).
2. Zutić, I., Fabian, J. & Sarma, S. D. Spintronics: fundamentals and applications. *Rev. Mod. Phys.* **76**, 323–410 (2004).
3. Herring, C. & Kittel, C. On the theory of spin waves in ferromagnetic media. *Phys. Rev.* **81**, 869–880 (1951).
4. Vonsovskii, S. V. *Ferromagnetic Resonance* (Pergamon, 1966).
5. Zhang, Z., Hammel, P. C. & Wigen, P. E. Observation of ferromagnetic resonance using magnetic resonance force microscopy. *Appl. Phys. Lett.* **68**, 2005–2007 (1996).
6. de Loubens, G. *et al.* Magnetic resonance studies of the fundamental spin-wave modes in individual submicron Cu/NiFe/Cu perpendicularly magnetized disks. *Phys. Rev. Lett.* **98**, 127601 (2007).
7. Hammel, P. C. & Pelekhov, D. V. *Handbook of Magnetism and Advanced Magnetic Materials* Vol. 5, Part 4 (Wiley, 2007).
8. Sidles, J. A. Folded Stern-Gerlach experiment as a means for detecting nuclear magnetic resonance in individual nuclei. *Phys. Rev. Lett.* **68**, 1124–1127 (1992).
9. Sidles, J. A. *et al.* Magnetic resonance force microscopy. *Rev. Mod. Phys.* **67**, 249–265 (1995).
10. Rugar, D., Yannoni, C. S. & Sidles, J. A. Mechanical detection of magnetic resonance. *Nature* **360**, 563–566 (1992).
11. Degen, C. L., Poggio, M., Mamin, H. J., Rettner, C. T. & Rugar, D. Nanoscale magnetic resonance imaging. *Proc. Natl Acad. Sci. USA* **106**, 1313–1317 (2009).
12. Jorzick, J. *et al.* Spin wave wells in nonellipsoidal micrometer size magnetic elements. *Phys. Rev. Lett.* **88**, 047204 (2002).
13. Gurevich, A. G. & Melkov, G. A. *Magnetization Oscillations and Waves* 199, 414 (CRC, 1996).
14. Slavin, A. & Tiberkevich, V. Spin wave mode excited by spin-polarized current in a magnetic nanocontact is a standing self-localized wave bullet. *Phys. Rev. Lett.* **95**, 237201 (2005).
15. Urban, R. *et al.* Perturbation of magnetostatic modes observed by ferromagnetic resonance force microscopy. *Phys. Rev. B* **73**, 212410 (2006).
16. Obukhov, Y. *et al.* Local ferromagnetic resonance imaging with magnetic resonance force microscopy. *Phys. Rev. Lett.* **100**, 197601 (2008).
17. Obukhov, Y., Pelekhov, D. V., Nazaretski, E., Movshovich, R. & Hammel, P. C. Effect of localized magnetic field on the uniform ferromagnetic resonance mode in a thin film. *Appl. Phys. Lett.* **94**, 172508 (2009).
18. Damon, R. W. & van de Vaart, H. Propagation of magnetostatic spin waves at microwave frequencies in a normally-magnetized disk. *J. Appl. Phys.* **36**, 3453 (1965).
19. Yukawa, T. & Abe, K. FMR spectrum of magnetostatic waves in a normally magnetized YIG disk. *J. Appl. Phys.* **45**, 3146 (1974).
20. Schlömann, E. Generation of spin waves in nonuniform magnetic fields. I. Conversion of electromagnetic power into spin-wave power and vice versa. *J. Appl. Phys.* **35**, 159–166 (1964).
21. Kakazei, G. N. *et al.* Spin-wave spectra of perpendicularly magnetized circular submicron dot arrays. *Appl. Phys. Lett.* **85**, 443–445 (2004).
22. Mewes, T. *et al.* Ferromagnetic resonance force microscopy studies of arrays of micron size permalloy dots. *Phys. Rev. B* **74**, 144424 (2006).
23. Kalinikos, B. A. & Slavin, A. N. Theory of dipole-exchange spin wave spectrum for ferromagnetic films with mixed exchange boundary conditions. *J. Phys. C* **19**, 7013–7033 (1986).
24. Klein, O. *et al.* Ferromagnetic resonance force spectroscopy of individual submicron-size samples. *Phys. Rev. B* **78**, 144410 (2008).

Supplementary Information is linked to the online version of the paper at www.nature.com/nature.

Acknowledgements We acknowledge financial support from the US Department of Energy through grant no. DE-FG02-03ER46054.

Author Contributions I.L. and Y.O. collected data; I.L., Y.O., D.V.P. and P.C.H. analysed data; G.X., F.Y., A.H., P.B. and D.V.P. fabricated samples and micromagnetic probe tips; and I.L., Y.O., D.V.P. and P.C.H. wrote the manuscript.

Author Information Reprints and permissions information is available at www.nature.com/reprints. The authors declare no competing financial interests. Readers are welcome to comment on the online version of this article at www.nature.com/nature. Correspondence and requests for materials should be addressed to P.C.H. (hammel@mps.ohio-state.edu).